N-doped ordered mesoporous carbons prepared by a two-step nanocasting strategy as highly active and selective electrocatalysts for the reduction of O_2 to H_2O_2

Reference:

Sheng Xia, Daems Nick, Geboes Bart, Kurttepeli Mert, Bals Sara, Breugelmans Tom, Hubin Annick, Vankelecom Ivo F.J., Pescarmona Paolo P..- N-doped ordered mesoporous carbons prepared by a two-step nanocasting strategy as highly active and selective electrocatalysts for the reduction of O_2 to H_2O_2

Applied catalysis : B : environmental - ISSN 0926-3373 - 176(2015), p. 212-224

DOI: http://dx.doi.org/doi:10.1016/j.apcatb.2015.03.049

N-doped ordered mesoporous carbons prepared by a two-step nanocasting strategy as highly active and selective electrocatalysts for the reduction of O_2 to H_2O_2

Xia Sheng[a,b°], Nick Daems[a°], Bart Geboes[c,d], Mert Kurttepeli[e], Sara Bals[e], Tom Breugelmans[c,d], Annick Hubin[c], Ivo F. J. Vankelecom[a] and Paolo P. Pescarmona[a,f*]

[a] *Centre for Surface Chemistry and Catalysis, University of Leuven (KU Leuven), Kasteelpark Arenberg 23, Heverlee, PO Box 2461, 3001, Belgium.*

[b] *School of Chemistry and Chemical Engineering, Henan University of Technology, Lianhua street 100, 450001 ZhengZhou, China.*

[c] *Vrije Universiteit Brussel, Research Group Electrochemical and Surface Engineering, Pleinlaan 2, 1050 Brussels, Belgium.*

[d] *University of Antwerp, Research Group Advanced Reactor Engineering, Salesianenlaan 30, 2660 Hoboken, Belgium.*

[e] *EMAT, University of Antwerp, Groenenborgerlaan 171, B-2020 Antwerp, Belgium.*

[f] *Chemical Engineering Department, University of Groningen, Nijenborgh 4, 9747 AG Groningen, The Netherlands.*

[*] *Corresponding author. Email: P.P.Pescarmona@rug.nl*

[°] *These authors contributed equally.*

Abstract

A new, two-step nanocasting method was developed to prepare N-doped ordered mesoporous carbon (NOMC) electrocatalysts for the reduction of O_2 to H_2O_2. Our strategy involves the sequential pyrolysis of two inexpensive and readily available N and C precursors, *i.e.* aniline and dihydroxynaphthalene (DHN), inside the pores of a SBA-15 hard silica template to obtain N-doped graphitic carbon materials with well-ordered pores and high surface areas (764 and 877 m^2/g). By tuning the ratio of carbon sources to silica template, it was possible to achieve an optimal filling of the pores of the SBA-15 silica and to minimise carbon species outside the pores. These NOMC materials displayed outstanding electrocatalytic activity in the oxygen reduction reaction, achieving a remarkably enhanced kinetic current density compared to state-of-the-art N-doped carbon materials (-16.7 mA cm^{-2} at -0.35V vs. Ag/AgCl in a 0.1 M KOH solution as electrolyte). The NOMC electrocatalysts showed high selectivity towards the two-electron reduction of oxygen to hydrogen peroxide and excellent long-term stability.

Keywords

N-doped ordered mesoporous carbon, two-step synthesis, metal-free electrocatalyst, oxygen reduction reaction, hydrogen peroxide.

1. Introduction

The development of suitable technologies for the sustainable conversion of energy is a crucial challenge faced by the human society. Fuel cells are very attractive power sources with applications ranging from stationary power generation in industry to portable power for mobile applications. The high efficiency of fuel cells stems from the conversion of the chemical energy of a thermodynamically favourable reaction into electricity. A commonly used reaction for this purpose involves the oxidation of hydrogen and the reduction of oxygen, with water as the product. The electrochemical reduction of O_2 to H_2O occurs through the transfer of four electrons (1), whereas the partial reduction of O_2 to H_2O_2 involves the transfer of two electrons (2).

$O_2 + 4\ H^+ + 4\ e^- \rightarrow 2\ H_2O$ (*acidic env.*) $E^0 = 1.23$ V (1)
$O_2 + 2\ H_2O + 4\ e^- \rightarrow 4\ OH^-$ (*basic env.*) $E^0 = 0.40$ V

$O_2 + 2\ H^+ + 2\ e^- \rightarrow H_2O_2$ (*acidic env.*) $E^0 = 0.70$ V (2)
$O_2 + H_2O + 2\ e^- \rightarrow HO_2^- + OH^-$ (*basic env.*) $E^0 = -0.06$ V

The oxygen reduction reaction (ORR) is not only important for H_2-O_2 fuel cells but also for direct methanol fuel cells and for metal-air batteries. Since the kinetics of the cathodic ORR are sluggish compared to the anodic reaction, research efforts have focussed on the development of active, selective and cost-effective electrocatalysts for the cathode [1]. The selectivity of the electrocatalyst in the ORR is of prime importance. A high selectivity towards the 4-electron reduction of oxygen to water is desired if the target is to maximise the generation of electricity [1]. On the other hand, a highly selective 2-electron reduction to hydrogen peroxide can also be attractive because it would allow the cogeneration of a useful product and of electricity. This last approach can provide a sustainable and economically advantageous way to produce industrially relevant chemicals that are prepared through a redox reaction with $\Delta G < 0$ (*i.e.* $E > 0$), by converting the energy that is generally dissipated in the form of heat into electricity [2]. H_2O_2 is one of the most important chemical commodity products, used as a green oxidant in a large variety of applications [3]. However, because of the high cost and hazardous nature of its standard production through the anthraquinone process, the development of an environmentally friendly process based on hydrogen and oxygen as reactants is highly desired. The electrochemical approach has the relevant advantage of performing the reduction of O_2 and the oxidation of H_2 in two separate cells, thus avoiding the contact between the two reagents and making the process intrinsically safer compared to the direct reaction of H_2 with O_2. Different designs of H_2/O_2 fuel cells for the synthesis of H_2O_2 have been proposed, with the electrolyte being an acidic solution, a basic solution or a solid polymeric membrane [4, 5]. The latter option allows obtaining neutral and electrolyte-free solutions of H_2O_2. An essential factor for the development of fuel cells for the cogeneration of chemicals and electricity is the identification of suitable electrocatalysts. The choice of the electrocatalyst is crucial for obtaining high selectivity towards the 2-electron reduction of O_2 to H_2O_2 and to avoid further electrochemical reduction of H_2O_2 to H_2O by another 2-electron reduction (3) or the chemical disproportionation reaction of H_2O_2 (4) [6].

$H_2O_2 + 2\ H^+ + 2\ e^- \rightarrow 2\ H_2O$ (*acidic env.*) $E^0 = 1.76$ V (3)
$H_2O + HO_2^- + 2\ e^- \rightarrow 3\ OH^-$ (*basic env.*) $E^0 = 0.86$ V

$2\ H_2O_2 \rightarrow 2\ H_2O + O_2$ (4)

A variety of electrocatalysts has been developed for the oxygen reduction reaction, either to H_2O or to H_2O_2 [7-9]. The benchmark electrocatalysts for this reaction consist of noble metal particles, typically Pt, supported on carbon, which show high activity in terms of produced current and display high selectivity towards the full reduction of O_2 to H_2O [10-12]. Although the use of noble metals in the form of supported nanoparticles allowed increasing the efficiency of the electrocatalysts per gram of the very expensive metal, the cost and the stability of these materials still represent serious limitations for their practical application [13]. Therefore, alternative types of electrocatalysts have been sought. Initial attempts to replace Pt focused on the development of electrocatalysts based on non-noble metals. Pyrolysed carbon-supported transition metal complexes forming metal-N_x chelates (with $x = 2$ or 4; *e.g.* phthalocyanines) exhibited the most promising results in terms of ORR activity [14, 15]. However, these catalysts have two disadvantages: low stability and, in general, lower activity than Pt-based catalysts. Recently, nitrogen-doped carbon materials have drawn great interest as an alternative to conventional Pt-based electrocatalysts [16]. These metal-free materials can reach competitive electrocatalytic activity in the ORR and exhibit

long-term stability [17]. Their unique electronic properties are derived from the conjugation between the orbitals of the nitrogen lone-pair electrons and the graphitic π-system. N-doped carbon materials can be prepared in different morphologies, among which N-doped ordered mesoporous carbons (NOMCs) are particular attractive for catalytic applications because they are characterised by regular arrays of uniform mesopores that lead to a material with extremely high specific surface area (500-1900 $m^2 g^{-1}$) [13, 18, 19]. Moreover, the size of the pores in the mesocale (typically between 2 and 50 nm) is favourable for the diffusion of reactants and products through the catalyst [13]. As for all carbon materials, NOMCs combine high electrical and thermal conductivity with high stability.

In this work, we present a new nanocasting strategy for the synthesis of highly active, selective and stable N-doped ordered mesoporous carbon electrocatalysts for the reduction of O_2 to H_2O_2. The synthesis method is based on the use of two inexpensive and readily available carbon precursors, *i.e.* aniline and dihydroxynaphthalene (DHN), which are sequentially introduced into the pores of mesoporous SBA-15 silica as a hard template. In our strategy, the pores of SBA-15 are covered with a monolayer of aniline, which is then polymerised and pyrolysed, followed by filling of the remaining pores space with dihydroxynaphthalene, by another pyrolysis step and finally by the removal of the silica template (Figure 1). In this way, N-doping will be limited to the surface of the material. DHN was chosen to complete the filling of the pores of the SBA-15 template because it has an extensive aromatic structure, with the target of favouring the formation of a graphitic structure, and because its hydroxyl groups can easily interact with N through hydrogen bridges. The two hydroxyl groups can also react with the SBA-15 silanol groups that might still be available, leading to grafting of the aromatic species through a dehydration reaction [20]. Two NOMC materials were prepared by tuning the amount of DHN employed in the synthesis. The obtained materials presented the desired array of parallel channels leading to high specific surface area (up to 877 $m^2 g^{-1}$) and displayed excellent electrocatalytic properties in the oxygen reduction reaction to H_2O_2.

2. Experimental

2.1 Preparation of SBA-15

The SBA-15 hard template was prepared according to a procedure reported in literature [21] using triblock copolymer Pluronic P123 (BASF) as structure directing agent and tetraethylorthosilicate (TEOS, Acros Organics) as silica source in acidic solution. The molar ratio of the components in the synthesis mixture was 1 SiO_2: 0.0167 Pluronic P123: 1.05 glycerol: 9.2 HCl: 188 H_2O. All chemicals were used without further purification. In a typical synthesis, 1.8 g of P123 and 1.8 g of glycerol were stirred overnight at 35°C in a 1 M HCl aqueous solution prepared by diluting concentrated HCl (37%, VWR) with distilled water. Next, 3.87 g of TEOS was added dropwise to the solution, which was then stirred for 5 min. Afterwards, the mixture was allowed to react for 24 h at 35°C under static conditions followed by a hydrothermal treatment at 100°C for 24 h in a closed polypropylene bottle, again under static conditions. The solid products were collected by filtration, washed with distilled water, and dried at 80°C overnight. The resulting powders were gently ground and calcined at 550 °C for 5 h to remove the organic structure directing agent.

2.2 Preparation of the NOMC materials

The N-doped ordered mesoporous carbon (NOMC) materials were prepared using a two-step procedure. First, aniline was polymerised inside the pores of SBA-15. The amount of aniline employed in this step was chosen in order to cover the SBA-15

surface with an aniline monolayer. For this purpose, the molecular cross-sectional area (σ) of aniline was calculated to be equal to 31.0 $Å^2$ from the formula:

$$\sigma = f\left(\frac{M}{\rho N_A}\right)^{\frac{2}{3}}$$

where *f* is a constant, equal to 1.091 for a close-packed liquid monolayer, M is the molecular mass of aniline (93.13 g mol^{-1}), ρ is the density of aniline at 20 °C (1.02 g cm^{-3}) and N_A is the Avogadro constant ($6.022 \cdot 10^{23}$ mol^{-1}) [22]. The value of σ for aniline is very similar to that for benzene (30.7 Å²). However, for practical applications, the value of the cross-sectional area of benzene is generally corrected to 43 $Å^2$ [22]. We applied the same correction and used a value of 43 $Å^2$ for our calculations. Dividing the surface area of 0.5 g of SBA-15 (413 m^2) by 43 $Å^2$ we obtain that 1.6 mmol of aniline are needed to achieve a monolayer on the SBA-15 surface. Therefore, 0.15 ml (1.6 mmol, Janssen Chimica) of aniline and 0.44 g (1.9 mmol) of the radical initiator ammonium persulfate (APS, Sigma-Aldrich) were added to a suspension of 0.5 g of SBA-15 in 250 ml of a 0.5 M HCl aqueous solution, and stirred for 24 h in an ice bath. Afterwards, the solvent was removed in a rotary evaporator and the sample was dried in an oven at 100°C. The sample was then placed into a quartz U-tube where it underwent pyrolysis for 3 h at 900°C (with a heating rate of 3 °C min^{-1}) under N_2 flow (1 cm^3 s^{-1}). This low N_2 flow rate was chosen in order to avoid excessive vaporisation and loss of aniline. In the second step of the procedure, the obtained grey solid was mixed with the selected amount of 2,3-dihydroxynaphthalene (DHN, 98% Sigma-Aldrich, b.p. ~354°C, ρ = 1.33 g cm^{-3}) in acetone as a solvent (5 ml) and stirred for 24 h at room temperature. Two different amounts of DHN were used: 0.36 g (2.3 mmol, NOMC-L) or 0.46 g (2.9 mmol, NOMC-H), corresponding to a 1:1.4 and 1:1.8 molar ratio between aniline and DHN. After evaporation of the solvent, the composite material was thermally treated for 2 h at 300 °C under N_2 flow (3 °C min^{-1}, 1 cm^3 s^{-1}). Next, the sample was washed 3 times with acetone, collected by filtration and dried in a vacuum oven at 60°C. A final pyrolysis was then performed for 5 h at 900°C (heating rate: 3 °C min^{-1}) under N_2 flow (1 cm^3 s^{-1}). Finally, the silica template was removed by suspending the black solid in a 2.5 wt% NaOH solution in a 1:1 mixture of EtOH/H_2O while stirring for 8 h at 100°C under reflux and under N_2 flow. The NOMC material in the form of a black solid was then collected by filtration and dried for 24 h in a vacuum oven at 100°C.

In order to investigate the influence of DHN on the ORR activity, an extra electrocatalyst was prepared following the same procedure described above but without the addition of DHN (NOMC-no-DHN).

2.3 Physicochemical characterisation of the NOMC materials

Small-angle X-ray scattering (SAXS) patterns of the NOMCs were recorded at room temperature by using a SAXSess mc^2 instrument (Anton Paar, Graz, Austria) with line-collimated Cu*Kα* ($\lambda_{K\alpha}$ = 0.154 nm) radiation and a 2D imaging plate detector. "SAXSquant" software was used to model the subtraction of the background (empty sample holder) [23]. The SAXS patterns were plotted as a function of 2θ. The 2θ value is related to the scattering vector (q, in nm^{-1}), which is often used in SAXS patterns, by the following equation: $q = 4\pi\sin(\theta)/\lambda$ [24]. Wide-angle X-ray diffraction (XRD) patterns were measured on a STOE Stadi P instrument using Cu*Kα* radiation. Nitrogen adsorption–desorption isotherms were measured at 77 K on a Micromeritics Tristar 3000. The pore size distributions were determined using the Barrett-Joyner-Halenda (BJH) method applied to the adsorption branch of the isotherm, whereas the Brunauer-Emmett-Teller (BET) method was used to calculate the surface area of the samples [25]. The Dumas-method was used for elemental analysis to determine the percentages of N and C: the NOMC materials were subjected to an oxidative combustion process at 900 °C, and the produced gases were detected with

a thermal conductivity detector (Vario Max CN, Elementar) [26]. Transmission electron microscopy was done partly at EMAT, and partly at MTM-KU Leuven, using a FEI Tecnai G2 operated at 200 kV (EMAT) and a Philips FEG CM200 operated at 200 kV, respectively. Samples were prepared by dispersing the powders in ethanol and placing several drops of the dispersion onto a holey carbon grid. The samples were visualised using electron tomography, performed by collecting a tilt series of 2-dimensional images using high-angle annular dark-field scanning transmission electron microscopy (HAADF-STEM) over an angular range of ±72° with a tilt increment of 2°. After the alignment of the projection images, a 3-dimensional reconstruction was obtained using the simultaneous iterative reconstruction technique (SIRT) [27] implemented in the FEI Inspect3D software. X-ray photoelectron spectroscopy (XPS) was used to determine the elemental composition at the surface of the NOMCs and to give information about the molecular environment of the different atoms. The analysis was carried out on a Physical Electronics PHI 1600 multi-technique system using an Al $K\alpha$ (1486.6 eV) monochromatic X-ray source, which was operated at 15 kV and 150W at a pressure of $2 \cdot 10^{-9}$ Torr. The graphitic C 1s band at 284.6 eV was taken as internal standard, in order to correct possible deviations caused by electric charging of the samples. The multipack software was used for the deconvolution and integration of the XPS spectra. Room-temperature Raman spectra were recorded on a LabRAM HR Evolution-Horiba Scientific system with a green laser (532 nm). Deconvolution and peak integration was performed by using the PeakFit v4.12 software.

2.4 Electrochemical characterisation of the NOMC materials

The electrocatalytic activity of the NOMCs in the oxygen reduction reaction was evaluated by means of rotating disc electrode (RDE) linear sweep voltammetry (LSV). The commercially available Pt/C (20 wt% Pt on Vulcan XC 72 purchased from Alfa Aesar), which is commonly employed as benchmark electrocatalyst for the ORR, was used as a reference for comparison with the synthesised NOMCs [28]. LSV measurements were conducted at various rotating speeds (400 to 2500 rpm). The experiments were carried out at room temperature in a conventional three-electrode cell with a Radiometer EDI-101 rotating disc electrode connected to an Autolab PGSTAT 302F potentiostat. An Ag/AgCl (saturated KCl) reference electrode was used in combination with a Pt counter electrode. The reference electrode has an internal salt bridge filled with 0.1 M KOH. A Luggin capillary is present between the compartment of the reference electrode and the working electrode. A glassy carbon RDE (with a surface area of 0.283 cm^2) was employed as an inert carrier for the working electrode. Catalyst ink solutions were prepared by suspending 2 mg of electrocatalyst powder in 1.5 ml of solvent (1:1 volume mixture of isopropanol and H_2O). 5 µl of catalyst ink was then deposited onto the glassy carbon surface, yielding an approximate catalyst loading of 25 µg cm^{-2}. After drying, a thin Nafion film was applied by depositing 7 µl of a 0.05 wt% Nafion solution (diluted with 1:1 isopropanol with water from a 5 wt% Nafion solution in a mixture of perfluorosulfonic acid with lower aliphatic alcohols from Aldrich) followed by a final drying step at room temperature. The ORR was performed under alkaline conditions using an aqueous 0.1 M KOH electrolyte solution saturated with O_2. The saturation of the electrolyte solution with O_2 was achieved by bubbling O_2 gas for 10 min, after which O_2 flow was maintained just above the solution during the whole voltammetric measurement. The potential was varied from 0.2 to -1.2 V vs. Ag/AgCl at a potential sweep rate of 10 mV s^{-1}. Before each blank measurement, N_2 was bubbled into the electrolyte solution for 30 min, in order to remove the remaining O_2.

Cyclic voltammograms (CV) of NOMC-H and NOMC-L were recorded on a glassy-carbon electrode in either N_2-saturated or O_2-saturated 0.1 M KOH aqueous solutions, by varying the potential between 0.2 and -1.0 V at a scan rate of 50 mV s^{-1}.

Chronoamperometric tests were carried out at a fixed potential of -0.4 V in O_2-saturated 0.1 M KOH at a rotation rate of 1600 rpm during 5 h. The features of the cell and the preparation of the working electrode were as in the LSV experiments (*vide supra*).

3. Results and discussion

3.1 Synthesis and physicochemical characterisation of the NOMC electrocatalysts

A novel, two-step nanocasting method was designed and applied to the synthesis of N-doped ordered mesoporous carbon (NOMC) materials using readily available and inexpensive N and C sources (aniline and 2,3-dihydroxynaphthalene). The synthesis of N-doped mesoporous carbons by nanocasting typically consists in filling the pores of an inorganic solid template with suitable C and N precursors, followed by pyrolysis and removal of the inorganic template to produce a carbon negative, *i.e.* a material in which the carbon part corresponds to the pores of the inorganic template and the voids correspond to the walls of the template [28-30]. For application as electrocatalysts for the ORR, highly aromatic large molecules (*e.g.* porphyrin derivatives) have been employed as precursors for the formation of the ordered carbon framework [13, 28]. The NOMCs prepared with this approach display excellent ORR activity but the high price and often complex synthesis of highly aromatic large molecules represent a serious limitation for the up-scaling of the fabrication of these NOMCs. Therefore, the development of an accessible and affordable method for the synthesis of NOMCs with enhanced electrocatalytic performance in the oxygen reduction reaction (ORR) is a highly attractive target. Our two-step synthetic procedure is illustrated in Figure 1. This original strategy differs from the known nanocasting methods because it aims at generating a carbon material in which N-doping is mainly occurring at the surface and with a carbonaceous core having high graphitic degree, which would provide high electrical conductivity. For this purpose, an N precursor (aniline) and a C precursor (2,3-dihydroxynaphthalene) were sequentially introduced and pyrolysed into the pores of SBA-15 mesoporous silica, which is widely used as hard template for nanocasting [13]. Aniline was selected as N-containing precursor because it can be easily polymerised and it contains an aromatic ring in its structure. DHN was employed to complete the filling of the SBA-15 pores because it has a more extended aromatic structure compared to aniline, and this feature is expected to facilitate the graphitisation process upon pyrolysis [31]. Both molecules can be easily introduced into the pores of the template as their size is small compared to that of the mesopores of SBA-15. Moreover, the polymerisation of aniline, the high boiling point of DHN (~354°C) and the ability of these compounds to interact with each other and with the silanol groups at the surface of SBA-15, are all expected to promote carbonisation over evaporation during the pyrolysis steps [32]. SBA-15 was chosen as template for the nanocasting because it displays high specific surface area originating from its hexagonal array of parallel mesopores, and can be prepared with micropores connecting the parallel channels. This latter feature is essential for the generation of ordered mesoporous carbon structures because it leads to the formation of carbon bridges that prevent agglomeration of the carbon rods after removal of the silica template (Figure 1), thus leading to a carbon material with high surface area [13]. The textural features of the prepared SBA-15 were characterised by N_2-physisorption (Table 1 and Figure 2). The material presents the anticipated high surface area and the desired combination of meso- and micropores. Transmission electron microscopy (TEM) confirms the successful formation of the characteristic hexagonal array of parallel mesopores of SBA-15 (Figure 3.A). In the next step, aniline was introduced into the pores of SBA-15, and then polymerised.

The added amount of aniline was chosen to form only an adsorbed monolayer on the pore walls of SBA-15, with the aim of achieving an N-containing carbon layer after pyrolysis at 900 °C. The obtained material was impregnated with 2,3-dihydroxynaphthalene (DHN), after which a self-assembly dehydration reaction occurred in the pores at 300 °C under N_2. A careful tuning of the amount of DHN is essential to achieve a complete filling of the pores with DHN, while avoiding an excessive loading that would lead to the formation of carbonaceous species outside the pores of the silica template. For this purpose, two different amounts of DHN were employed, leading to a sample prepared with lower amount of DHN (NOMC-L, with a 1:1.4 molar ratio between aniline to DHN) and one with higher amount (NOMC-H, with a 1:1.8 molar ratio between aniline and DHN). These amounts were calculated based on the total pore volume of the SBA-15 (Table 1) minus the volume of aniline that was added in the first step, and considering that part of the aniline employed in the first step is lost at 350-400 °C during the heating-up phase of the thermal treatment at 900 °C. After a second treatment at 900 °C to pyrolyse the DHN precursor, the silica template was removed by treatment with a NaOH solution that induces the conversion of the Si-O-Si bonds into Si-OH and $Si-O^-$ species [33]. The successful removal of the silica template was confirmed by XPS analysis (see Table 2).

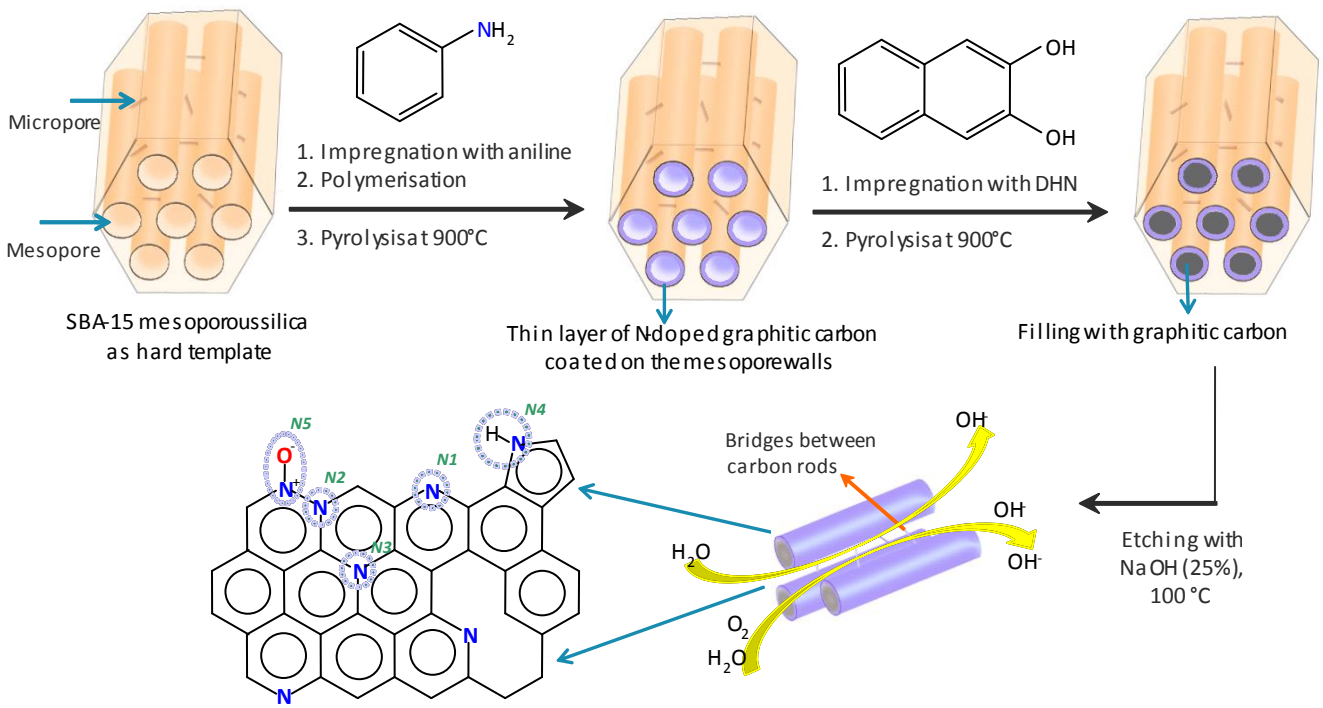

Figure 1. Schematic illustration of the formation of a NOMCs with a layer of N-doped carbon at the surface and a fully carbonaceous core, using SBA-15 as hard template. The possible configurations of N atoms in the NOMC material are indicated: pyridinic N (*N1*), graphitic N (*N2-N3*), pyrrolic N (*N4*) and oxidised pyridinic N (*N5*).

Table 1. Structural and textural properties of SBA-15 and NOMCs

	S_{BET}[a] (m^2/g)	Total pore volume[b] (cm^3/g)	Micropore Volume[c] (cm^3/g)	Mesopore Volume[d] (cm^3/g)	Pore size[b] (nm)	d_{100}[e] (nm)	a_0[f] (nm)	Wall thickness[g]
SBA-15	826	0.76	0.12	0.64	7.5	10.7	12.4	4.9
NOMC-H	877	0.56	0.06	0.50	3.3	9.0	10.3	7.0
NOMC-L	764	0.54	0.01	0.53	3.3	9.0	10.3	7.0
NOMC-no-DHN	761	0.78	0.06	0.72	4.3	n.d.	n.d.	n.d.

[a] S_{BET}: BET surface area. [b] Total pore volume and pore size determined by the BJH method. [c] Micropore volume, calculated by the t-plot method (Figure S.1) [34]. [d] Mesopore volume = total pore volume - micropore volume. [e] d-spacing calculated on the basis of the following formula $\lambda = 2d_{100}\sin\theta$. [f] Unit cell constant calculated by the equation $a_0 = 2d_{100}/\sqrt{3}$, where d_{100} is the spacing of the (100) planes of a hexagonal array of pores. [g] Wall thickness = a_0 - pore size.
n.d. = not determined.

The employed synthesis strategy was successful for preparing the desired N-doped ordered mesoporous carbon (NOMC) materials with a well-defined ordered carbon framework and high specific surface area, as demonstrated through a combination of characterisation techniques. The BET surface areas of NOMC-H and NOMC-L determined by N_2-physisorption are high among NOMCs prepared by introducing an N-containing carbon source in SBA-15 (*in-situ* method) [28, 35], reaching a value of 877 $m^2\ g^{-1}$ for NOMC-H (Table 1). These high surface areas are ascribed to the tuning of the amounts of the N and C precursor relative to the amount of silica template. The analogous adsorption-desorption isotherms of the two NOMC samples (Figure 2) are of type IV with a clear hysteresis loop at $p/p^0 = 0.4$-0.9, indicating the mesoporous character of the materials [32, 36]. The insets show narrow pore size distribution curves, corresponding to a rather uniform mesopore size around 3.3 nm (Table 1). The formation of the hexagonal arrays of parallel carbon rods with a regular spacing is unequivocally demonstrated by the TEM images (Figure 3.B and D) and by electron tomography (Figure 4.A and B) of NOMC-H and NOMC-L. The tomography data also allowed building a three-dimensional visualisation of the structure of NOMC-L (a video based on these tomography data is available as Supporting Information (Video S.1)). The presence of graphitic layers within the aligned carbon rods was evidenced by HR-TEM (Figure 4.C and D). These graphitic layers are organised in small, local domains, without a preferential orientation of the domains within the rod. The parallel array of long channels of NOMC-H and NOMC-L evidenced by TEM corresponds to long tubular carbon structures when observed on the micrometer scale by SEM (Figure 5). Besides the desired ordered mesoporous carbon framework, the TEM images of the NOMCs evidence the presence of small areas of unstructured carbon. These species probably originate from DHN that remained outside the pores of SBA-15 during the synthesis. Indeed, these disordered carbon species are observed in larger amount in NOMC-H, for which a higher ratio of DHN to aniline was employed (compare B and C with D and E in Figure 3). This observation can be related to the larger micropore volume of NOMC-H (Table 1), originating from the pyrolysis of DHN that was not confined into the silica pores, whereas the mesopore volume of the two NOMC materials is similar. The presence of this microporosity also explains the higher surface area of NOMC-H compared to NOMC-L (877 $m^2\ g^{-1}$ vs. 764 $m^2\ g^{-1}$).

The 2D-hexagonal ordering of the prepared NOMCs was confirmed by SAXS (Figure 6.A). The typical SAXS pattern of the SBA-15 silica used as template corresponds to a 2D-hexagonal P6mm space group with a strong peak correlated with the

(100) plane at 0.84° and two other weak peaks due to the (110) and (200) planes at 1.44° and 1.66°, respectively. The SAXS patterns of the NOMCs also show the characteristic diffraction peaks corresponding with the ordered hexagonal structure. However, these signals have a low intensity and the reflections of the (110) and (200) planes are almost indiscernible: this can be caused by a lower degree of order in the structure of the NOMCs compared to that of SBA-15 or by 'accidental extinctions' related to the specific sizes of the rods and pores [37, 38]. The (100) peaks of the NOMCs are shifted to higher 2θ value (0.97°) compared to that of SBA-15, corresponding to a d-spacing of 9.0 nm for the NOMCs and of 10.7 nm for SBA-15 (Table 1). The smaller d-spacing of the NOMCs is related to a shrinkage of the framework of the material during pyrolysis and upon dissolution of the silica template [39]. Since the mesoporous carbon material is produced inside the SBA-15 channels, the diameter of the carbon rods should correspond to the pores of SBA-15 whereas the voids of the resulting NOMC originate from the SBA-15 walls after removal of the silica template. Indeed, the diameter of the carbon rods (7 nm) matches well with the mesopore size of the SBA-15 (7.5 nm), whereas the voids of the NOMCs (3.3 nm) are smaller compared to the wall thickness of the silica template (4.9 nm), as a consequence of the above-mentioned shrinkage.

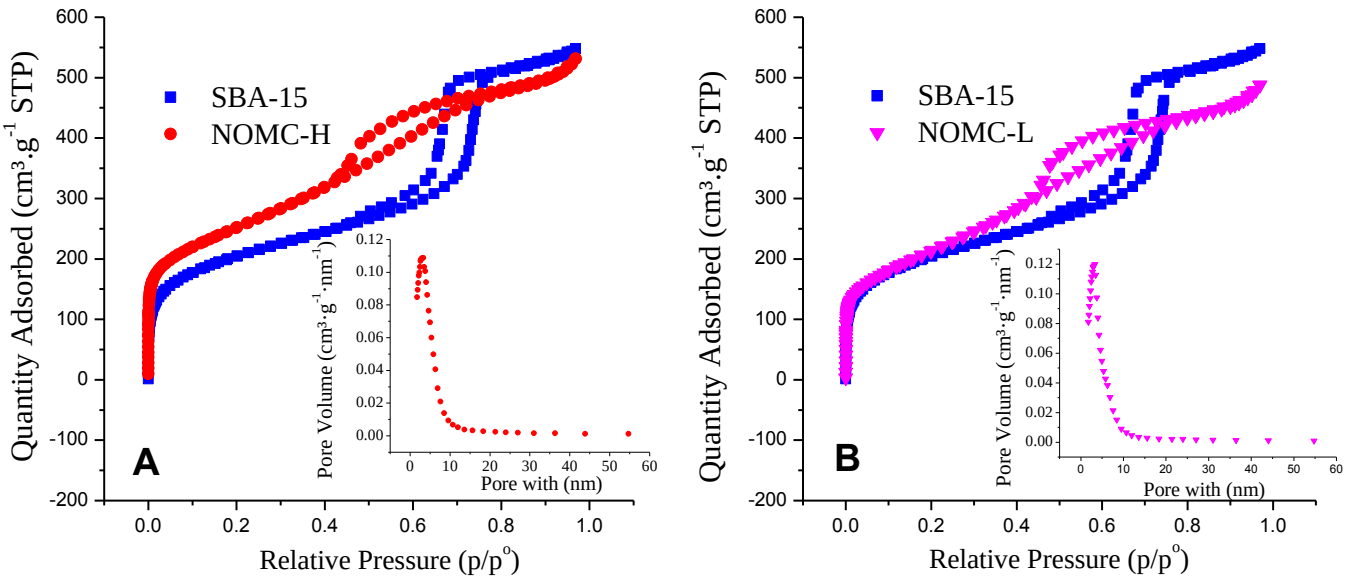

Figure 2. N_2 adsorption-desorption isotherms of NOMC-H (A) and NOMC-L (B) compared with the SBA-15 hard template. The insets are the respective BJH pore size distributions.

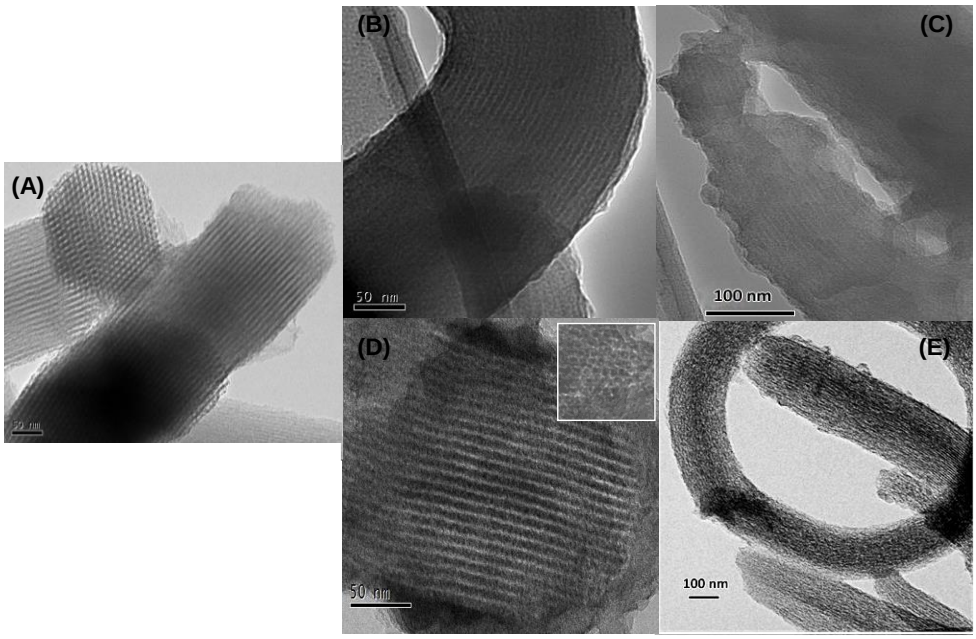

Figure 3. TEM images of: SBA-15 (A); NOMC-H (B and C); NOMC-L (D and E). The inset in (D) is the enlarged area of a top view of the hexagonal array of mesopores.

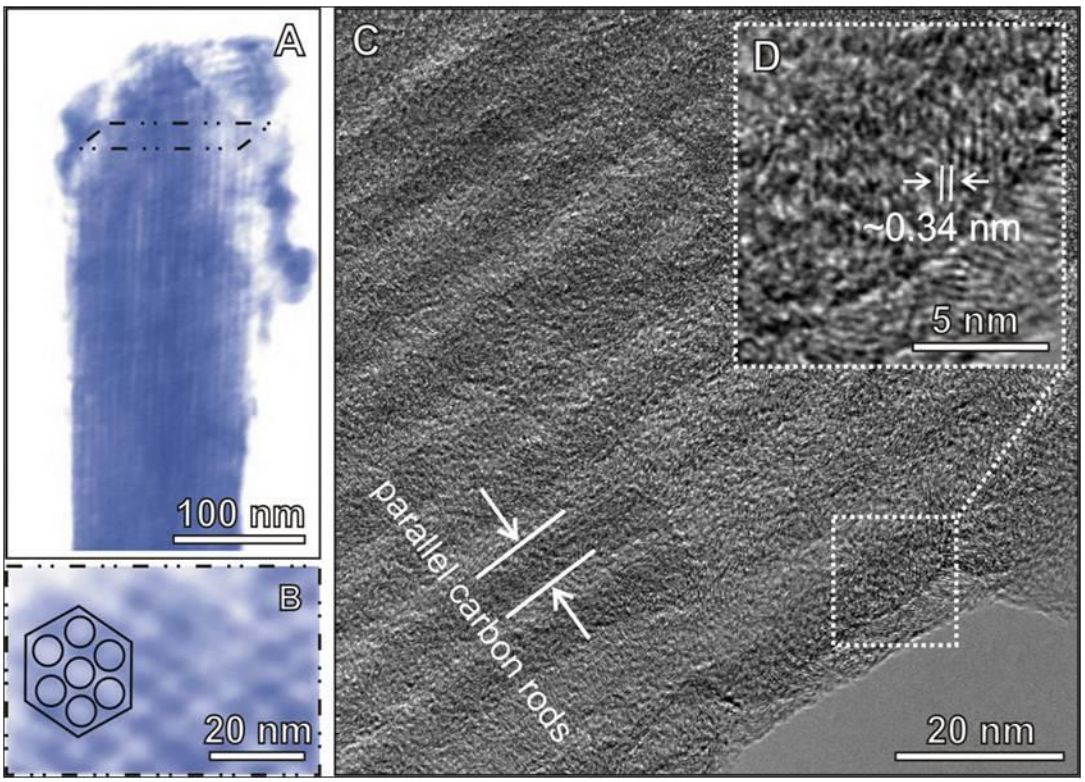

Figure 4. Reconstructions by electron tomography of the NOMC-L sample along different orientations (A and B). HR-TEM images of NOMC-L (C and D), with indication of the position of the parallel carbon rods and of the graphitic layers (~0.34 nm spacing).

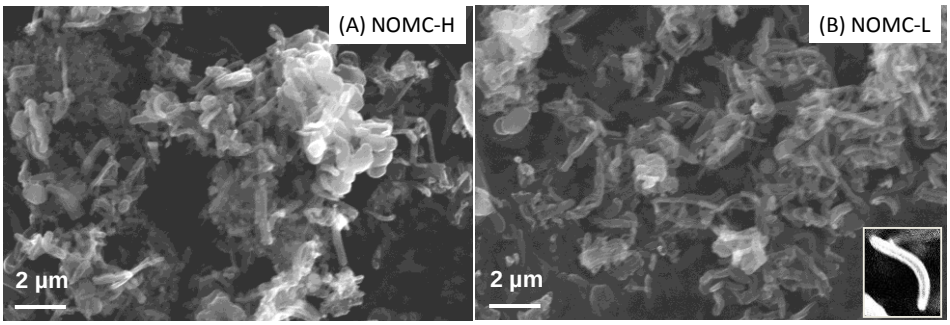

Figure 5. SEM images of NOMC-H (A) and NOMC-L (B). The inset is a zoomed image of a single tubular carbon structure.

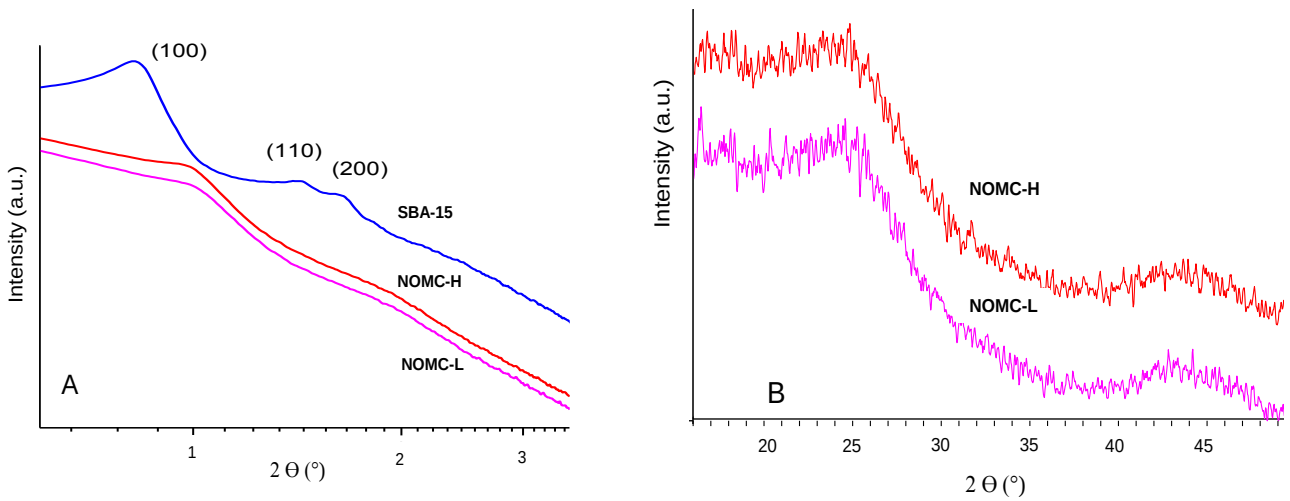

Figure 6. SAXS patterns of SBA-15 and of the NOMCs (A) and XRD patterns of the NOMCs (B).

The formation of an electrically conductive graphitic structure within the carbon rods of the NOMC materials would be an asset in view of an electrocatalytic application. The two peaks at 24.1° and at 42.3° in the wide-angle XRD patterns of the synthesised NOMCs (Figure 6.B) are characteristic for the (002) and (101) graphitic planes, respectively. As expected considering the nanoscale of the rods constituting the NOMCs and the HR-TEM data discussed above, the two peaks are rather broad, indicating a relatively low degree of crystallinity of the graphitic carbon structure [39]. Complementary information about the degree of graphitisation of the NOMCs is provided by Raman spectroscopy (Figure 7). The formation of graphitic structures within the carbon framework is clearly evidenced by the presence of an intense and narrow band at 1604 cm^{-1} (G-band), which is assigned to the planar C=C stretching vibration mode in an ideal graphitic layer. The position of this band is shifted to lower wavenumbers in N-doped carbon materials compared to undoped carbons, due to a change in the electronic structure of the carbon framework originating from n-type doping [13]. The other band at 1330 cm^{-1} (D-band) is correlated with structural defects and disordered structures at the edges of the sp^2 domain. The ratio of the areas of the D and G bands (I_D/I_G) is inversely proportional to the graphitic degree. The I_D/I_G values of NOMC-H and NOMC-L, *i.e.* 1.5 and 1.3 (Table 2), are in the same range as N-doped carbon nanotubes and relatively high compared with previously reported N-doped graphite [13]. This confirms that the rods constituting the NOMCs have a graphitic character, though the graphitisation degree is lower

compared to the extensive layers of graphite. The higher graphitic degree of NOMC-L compared to NOMC-H shows that the higher amount of DHN employed in the synthesis of the latter material generated a less graphitic structure, which could correspond to the disordered carbon species observed by TEM (*vide supra*). Besides the two major G- and D-bands, deconvolution of the Raman spectra indicates the presence of two additional peaks centred at 1200 and 1510 cm^{-1} (Figure 7), which are respectively attributed to carbon atoms outside a perfectly planar graphitic network (such as aliphatic species) and to five-member rings or heteroatoms integrated in the graphite sheet [40]. In line with the lower graphitic degree of NOMC-H mentioned above, the relative contribution of these two bands is slightly higher for NOMC-H than for NOMC-L. Although the graphitic degree of the two NOMC materials is lower compared to graphite, impedance measurements performed on glassy carbon disc electrodes coated with an ink of NOMC-H, NOMC-L or graphite showed that the electrical resistance of the electrodes based on the NOMC materials lies in the same range as that of an electrode based on pure graphite under the employed experimental conditions (Table S.1).

Table 2. Carbon, nitrogen and oxygen contents and I_D/I_G ratio of the prepared NOMCs.

	C (wt%)[a]	N (wt%)[a]	O (wt%)[a]	Si (wt%)[a]	I_D/I_G[b]
NOMC-H	87	3.0 (theor. 3.6)	9.7	< 1	1.5
NOMC-L	87	3.4 (theor. 4.3)	9.2	0.0[c]	1.3
NOMC-no-DHN	87	5.7 (theor. 15.0)	6.7	1.0	n.d.

[a]Determined by XPS. [b]Determined from the deconvolution of the Raman spectra (measured with a laser with $\lambda = 532$ nm). [c] No Si signal was detected.
n.d. = not determined .

The composition of the NOMCs and the configuration of the N atoms were investigated by means of X-ray photoelectron spectroscopy (XPS). The higher N-content of NOMC-L compared to NOMC-H (Table 2) is a direct consequence of the higher aniline to DHN ratio employed in the former. For both NOMC materials, the N-contents measured by XPS are lower than the theoretical value. This is attributed to the observed partial loss of aniline/polyaniline during pyrolysis (*vide supra*). Nitrogen can occupy different sites within the graphitic structure of carbon materials (*N1-N5* in Figure 1) [17]. Each of these nitrogen bonding configurations can be characterised based on the position of the N1s peaks in the XPS spectrum of the N-doped carbon material. The N1s signal can be deconvoluted into four peaks (Figure 8), which are assigned to pyridinic N (398.5 eV, *N1*), pyrrolic N (400.5 eV, *N4*), graphitic N (401.1 eV, *N2* and *N3*) and oxidised pyridinic N (> 402.8 eV, *N5*) [40, 41]. Both graphitic and pyridinic N atoms have been proposed to be involved in the electrocatalytic activity of N-doped carbon materials in the ORR, but the exact nature of the active sites is still debated [1, 13, 42, 43]. Our NOMC materials present graphitic and pyridinic N atoms as the two major species, with the former being more abundant, and show similar relative amounts of each of the N-configurations (Table 3).

The NOMC materials discussed above were prepared with a tailored strategy involving the sequential addition and pyrolysis of aniline and dihydroxynaphthalene. To investigate whether the use of DHN in the synthesis is essential, we prepared a reference material following the same procedure used for NOMC-H and NOMC-L but without the addition of DHN (NOMC-no-DHN). The obtained material also displays an ordered, hexagonal array of carbon rods (Figure S.2) and high specific surface area with a narrow pore size distribution centred at 4.3 nm (Table 1 and Figure S.3). The absence of DHN as precursor might lead to an incomplete filling of the carbonaceous rods, which fits with the larger micropore volume of NOMC-

no-DHN compared to NOMC-L (Table 1). The fact that NOMC-no-DHN was prepared using exclusively aniline as precursor implies that this material has a larger N-content compared to NOMC-H and NOMC-L, as proven by XPS analysis (Table 2 and Figure S.4). The deconvolution of the N1s signal of NOMC-no-DHN shows that this material contains a larger fraction of graphitic N and a lower fraction of pyridinic N compared to the other NOMCs (Table 3 and Figure S.4). It can be concluded that DHN does play an important role in the synthesis of the NOMC material. The physicochemical differences between these NOMCs are reflected by their different electrocatalytic performance, which will be discussed in the following section.

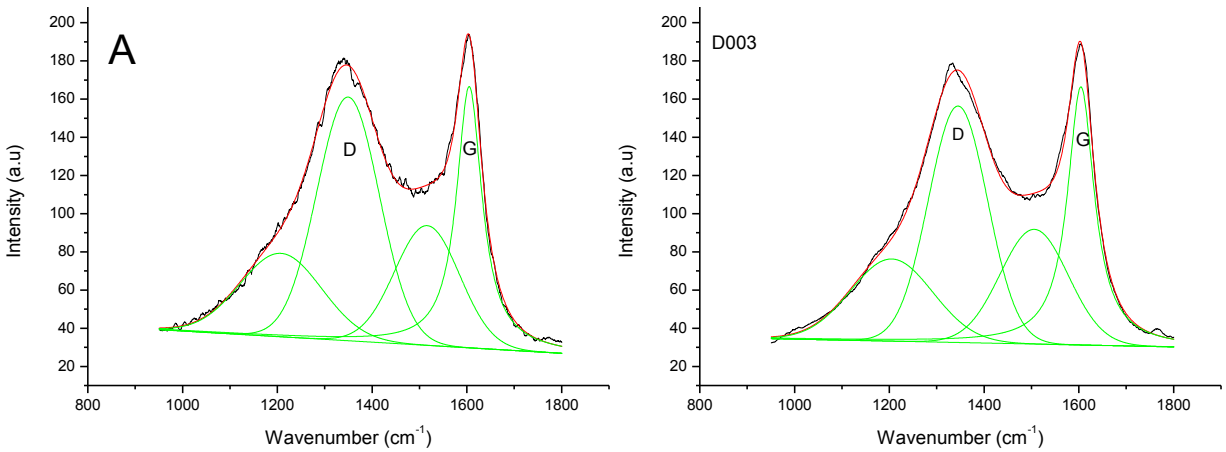

Figure 7. Deconvoluted Raman spectra for NOMC-H (A) and NOMC-L (B).

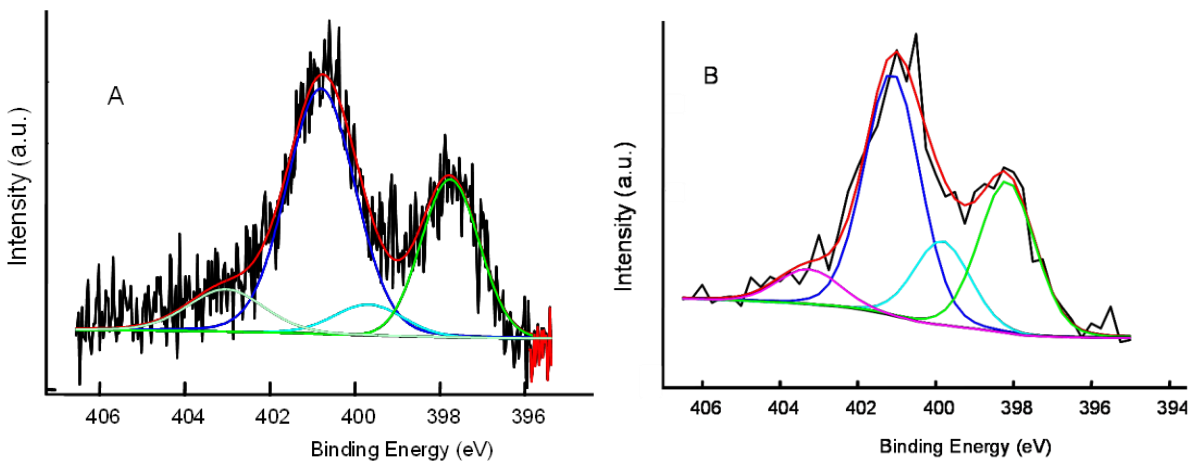

Figure 8. Deconvolution of the N1s XPS peak of NOMC-H (A) and NOMC-L (B).

Table 3. Binding energies (B.E.) and relative amounts of the various N species in the NOMCs.

	Pyridinic N (398-399.3 eV)			Pyrrolic N (399.8-401.2 eV)			Graphitic N (401.1-402.7 eV)			Oxidised pyridinic N (> 402.8 eV)		
	B.E. (eV)	Area%	wt%	B.E. (eV)	Area%	wt%	B.E. (eV)	Area%	wt%	B.E. (eV)	Area%	wt%
NOMC-H	398.0	33	0.99	399.8	11	0.34	401.0	48	1.44	403.3	7.4	0.22
NOMC-L	398.2	29	1.00	399.8	16	0.55	401.1	47	1.60	403.3	7.3	0.25
NOMC-no-DHN	398.9	26	1.48	400.2	8.9	0.51	401.7	56	3.20	403.6	8.7	0.50
wt%: weight %.												

3.2 Electrocatalytic performance of the NOMC materials in the ORR

The electrocatalytic activity of N-doped carbon materials in the oxygen reduction reaction is generally attributed to the higher electronegativity of N compared to C, which leads to a polarisation of the C-N bonds into $C(\delta^+)$-$N(\delta^-)$, thus altering the electronic properties of the carbon material and creating sites for interaction with O_2 [41]. Moreover, the incorporation of nitrogen into the carbon material enhances its electron-donor properties [44]. Both graphitic N and pyridinic N have been proposed to contribute to the electrocatalytic activity of N-doped carbon materials, but the exact role of these two types of sites in the reaction mechanism and their influence on the selectivity towards the partial reduction to H_2O_2 or the complete reduction to H_2O are still a matter of debate [13, 45, 46]. The NOMC materials prepared with our two-step approach display promising features for electrocatalytic application in the ORR: they have high specific surface area and regular mesopores, a graphitic character and N atoms both in graphitic and pyridinic configuration. The performance of NOMC-H and NOMC-L as electrocatalysts for the ORR was studied in a three electrode cell set-up in an aqueous 0.1 M KOH solution. The first electrochemical analysis was performed by cyclic voltammetry (CV) under static conditions (Figure 9). CV curves obtained with both NOMCs show only the capacitive background of the electrochemical double layer if the electrolyte was saturated with an inert gas as N_2 (dotted curve in Figure 9) [47]. When O_2 was introduced in the solution, two reduction peaks appeared at -0.24 and -0.84 V vs. Ag/AgCl for NOMC-L, which are characteristic for a two-step oxygen reduction reaction, with two electrons being exchanged in each step [48]. Comparing the performance of NOMC-H with that of NOMC-L, it can be seen that the peaks are slightly shifted to less negative potentials for NOMC-L, implying a smaller ORR overpotential for NOMC-L compared to NOMC-H.

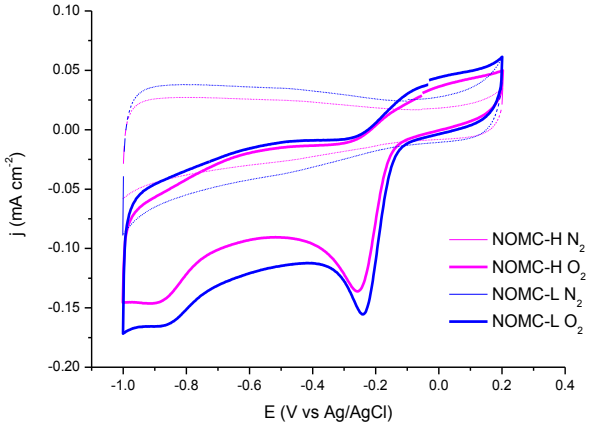

Figure 9. Cyclic voltammograms of NOMC-H and NOMC-L on a glassy-carbon RDE electrode in N_2 and O_2-saturated 0.1 M KOH solution between 0.2 and -1.0 V at a scan rate of 50 mV s^{-1}.

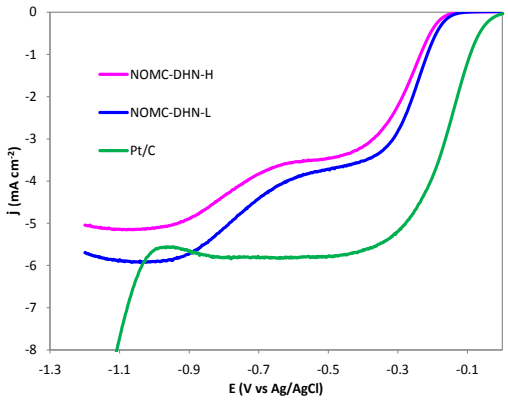

Figure 10. Linear sweep voltammograms for the NOMC electrocatalysts and for a standard Pt/C electrode, recorded in an O_2-saturated 0.1 M KOH solution at a scan rate of 10 mVs^{-1} and with a rotation speed of 2500 rpm.

The electrocatalytic behaviour of the two NOMCs was further investigated by linear sweep voltammetry (LSV) measurements at various rotation speeds, which were carried out in an O_2-saturated 0.1 M KOH solution in a three electrode cell set-up equipped with a rotating disc electrode (RDE). The kinetics of the reduction process for the two NOMCs were compared to those of a standard Pt/C electrocatalyst (20 wt% Pt on Vulcan XC 72, Alfa Aesar). The Pt/C electrocatalyst exhibited a one-step oxygen reduction pathway with an onset potential at 0.045 V vs. Ag/AgCl (Figure 10). In contrast, both NOMC electrocatalysts exhibit two reduction steps with a more negative onset potential, approximately -0.1 V for the first reduction and -0.6 V for the second reduction (Figure 10). The two NOMC electrocatalysts have similar yet slightly different onset potentials, indicating that the nature of their active sites is analogous. This is in agreement with the similar relative amounts of N atoms in each of the possible configurations in the two materials (*vide supra*). NOMC-L produces a higher diffusion-limited current than NOMC-H (Figure 10), which is correlated to the difference in the number of exchanged electrons at the plateau (-0.5 V vs Ag/AgCl). The number of transferred electrons (n) in the ORR over the investigated catalysts was calculated based on the Koutécky-Levich (K-L) equations (Eq. 1-3) [28]:

$$\frac{1}{J} = \frac{1}{J_K} + \frac{1}{J_D} = \frac{1}{J_K} + \frac{1}{B\omega^{1/2}} \qquad \text{(Eq. 1)}$$

where J is the measured current density, which is related to the kinetic current density (J_K) and the diffusion-limited current density (J_D), and ω is the angular velocity of the rotating electrode. B and J_K are given by Eq. 2 and 3:

$$B = 0.62nFC_0(D_0)^{2/3}\nu^{-1/6} \qquad \text{(Eq. 2)}$$

$$J_K = nFkC_0 \qquad \text{(Eq. 3)}$$

where F is the Faraday constant, k is the electron transfer rate constant (at a certain potential), C_0 is the bulk concentration of O_2 ($1.2 \cdot 10^{-6}$ mol cm^{-3}), v is the kinematic viscosity of the electrolyte ($0.01 cm^2\ s^{-1}$) and D_0 is the diffusion coefficient ($1.9 \cdot 10^{-5}\ cm^2\ s^{-1}$) [28].

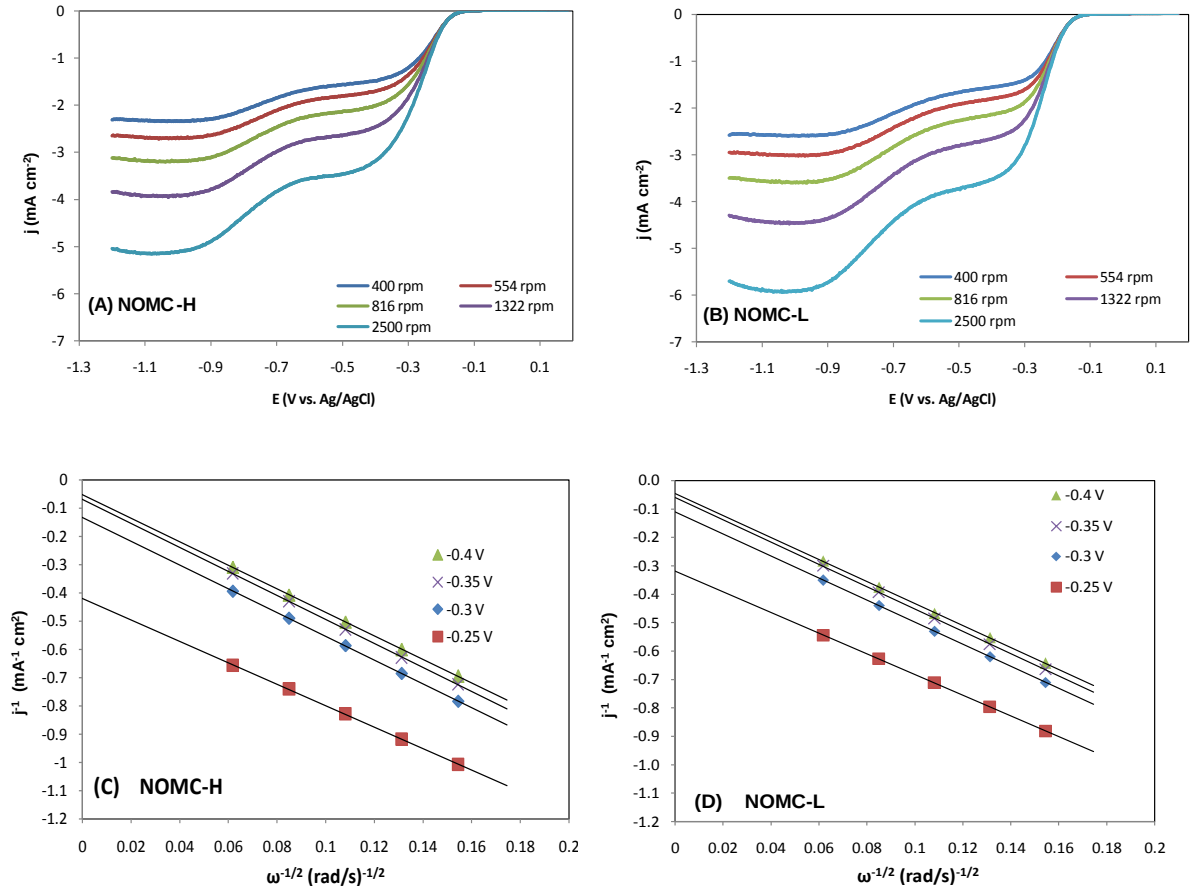

Figure 11. LSV curves for the NOMC electrocatalysts recorded in an O_2-saturated 0.1 M KOH solution with a scan rate of 10 mV s^{-1} at different rotation speeds (A and B), and the corresponding Koutécky-Levich plots (J^{-1} vs. $\omega^{-1/2}$) at different electrode potentials for NOMC-H (C) and NOMC-L (D).

K-L plots were generated on the basis of the LSV curves at various rotation speeds (Figure 11.A and B). The resulting K-L plots (Figure 11.C and D) for the two NOMC electrocatalysts at various potentials (from -0.25 to -0.4 V vs. Ag/AgCl) exhibit good linearity and all present very similar slopes, indicating a similar number of electrons transferred in the ORR in that potential range. The average number of exchanged electrons (n) calculated from the value of the slope using Eq. 2 was found to be 2.1-2.4 for the two NOMC materials in the selected potential range (Figure 12). These values are close to 2, indicating that H_2O_2 is produced with high selectively on our electrocatalysts. The first reaction step over the NOMCs is thus attributed to the reduction of O_2 to H_2O_2, which is an electrochemical intermediate, whereas the second step is assigned to the second 2-electron reduction reaction, where

H_2O_2 is further reduced to H_2O at the electrode [49]. A well-defined plateau corresponding to the diffusion-controlled region is observed for both NOMCs between -0.4 and -0.6 V vs. Ag/AgCl in the LSV plots. The presence of this plateau means that the two reduction steps are clearly separated over these NOMCs (no mixed reactions) [40]. In this work, the goal was to achieve high selectivity towards H_2O_2; hence the observed 2-electron exchange process is required. The formation of H_2O_2 during the LSV measurement was confirmed by the Merck peroxide test [16]. The number of exchanged electrons for the Pt/C catalyst was calculated to be 3.9-4.0 (Figure S.5), which demonstrates that the 4-electron reduction of O_2 to H_2O is the main reaction on this electrocatalyst, in agreement with previous reports [28, 50].

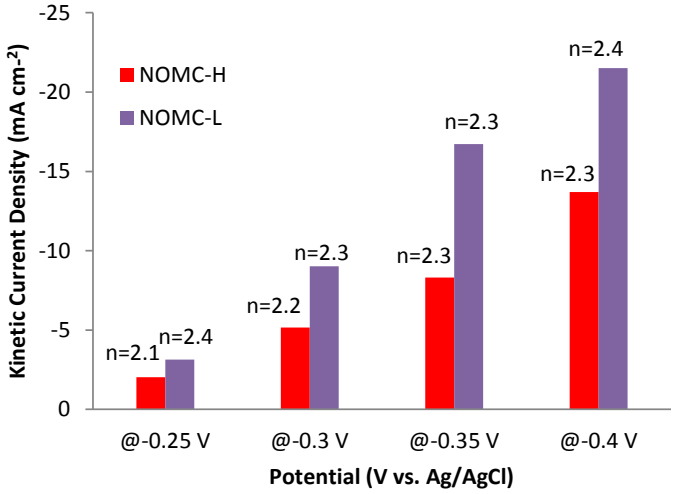

Figure 12. Kinetic current density and number of exchanged electrons for NOMC-H and NOMC-L at the selected potentials.

The activity of the electrocatalysts was evaluated on the basis of the kinetic current density in the mixed kinetics region (-0.25 to -0.4 V vs. Ag/AgCl, see Figure 12). The kinetic current density at a certain potential can be determined from the intercept of the K-L plots with the y-axis (Eq. 1). NOMC-L consistently shows a better performance than NOMC-H. For NOMC-L, a J_K of -16.7 mA cm^{-2} was obtained at -0.35 V vs. Ag/AgCl, which is twice as high as that of NOMC-H at the same potential (-8.3 mA cm^{-2}). The better electrocatalytic performance of NOMC-L compared to NOMC-H can be correlated to the physicochemical features of the two materials. NOMC-L has a higher N-content, a higher degree of graphitisation and a lower micropore volume compared to NOMC-H (Table 1 and 2). The higher N-content leads to the creation of more active sites, particularly considering that N is preferentially located at the surface of the material in our synthesis strategy. Graphitic and pyridinic N atoms are the most abundant configurations in both NOMC materials, in line with the proposed involvement of these species in the electrocatalytic activity of N-doped carbons [42]. The higher graphitic degree of NOMC-L is expected to lead to an increase in the electrical conductivity, and thus to promote a higher current density, but also to improve the durability of the electrocatalyst in the ORR [40]. Finally, it has been proposed that the ORR mainly occurs in the mesopores of the electrocatalyst, whereas micropores can be detrimental [51]. Furthermore, the unstructured carbon

species that were observed in larger amounts in NOMC-H could infiltrate into the mesopores when the catalyst powder is suspended into a solution during the electrode preparation process, and this could lead to partial blockage of the mesopores thus hindering the diffusion of the reactant to the active sites. Although the NOMC with the lower amount of DHN (NOMC-L) displays better electrocatlytic performance, the use of DHN in the synthesis method is very important for the ORR activity of the NOMC. This was demonstrated by preparing an NOMC using only aniline to cover the pore surface of the SBA-15 template (NOMC-no-DHN). Linear sweep voltammetry (Figure S.6) showed that the electrocatalytic performance of NOMC-no-DHN was markedly worse than that of the two NOMCs prepared by using DHN, as evidenced by the much lower absolute value of kinetic current density (Table 4). The inferior results obtained with NOMC-no-DHN can be correlated to the presence of microporosity and to the different relative amounts of N atoms with graphitic and pyridinic configuration compared to NOMC-H and NOMC-L (*vide supra*). Moreover, it has been reported that too high N-content can cause disruption of the π-system, thus reducing the electron conductivity of the material [13]. Therefore, the high N-content of NOMC-no-DHN might be detrimental to the ORR activity of the electrocatalyst. Further investigation would be required to determine the specific influence of each of these factors.

Table 4. Electrocatalytic properties of various N-doped carbon materials for the ORR in an alkaline electrolyte [all potentials are expressed vs. Ag/AgCl].

Entry	Electrocatalyst	J_k (mA/cm^2)	*n*	Onset potential (V vs. Ag/AgCl)
1	NOMC-H	-8.3 at -0.35 V	2.3	-0.1
2	NOMC-L	-16.7 at -0.35 V	2.3	-0.1
3	NOMC-no-DHN	-3.1 at -0.35 V	2.3	-0.1
4	Ref. graphene oxide [52]	-3.7 at -0.5 V	2.4	-0.2
5	Ref. N-graphene oxide [52]	-4.2 at -0.5 V	2.6	-0.2
6	Ref. NOMC-750 [28]	-7 at -0.35 V	2.6	-0.1
7	Ref. NOMC-900 [28]	-9 at -0.35 V	3.9	-0.1

Notably, the kinetic current density obtained with NOMC-L is not only superior to that with NOMC-H and NOMC-no-DHN, but also much higher (in absolute value) than that found with previously reported N-doped carbon materials (Table 4 and Figure 12) [28, 52, 53] including the state-of-the-art NOMC electrocatalyst prepared using a large aromatic dye molecule [28], which was tested under exactly the same conditions and with the same electrode loading (25 $\mu g_{catalyst}$ cm^{-2}) as used in this work. The improved kinetic current over NOMC-L compared to the NOMC from the literature is most likely caused by the higher surface area and the excellent ordering of the mesopores in NOMC-L, which both lead to an easier diffusion of O_2 through the pores and thus to enhanced accessibility of the active sites. The superior kinetic current density measured at -0.35 V over NOMC-L is even more remarkable when considering that at this potential the catalyst promotes a 2-electron reduction step (*n* = 2.3), while the best NOMC reported in the literature promotes a 4-electron reduction (*n* = 3.9, see entry 2 and 7 in Table 4). It can be concluded

that NOMC-L is an excellent electrocatalyst for the oxygen reduction reaction to H_2O_2. The high selectivity of our NOMC materials towards the reduction of molecular oxygen to H_2O_2 indicates that during the reduction process the O-O bond of the adsorbed O_2 is not weakened to the point of causing its rupture, and the desorption of H_2O_2 after the 2-electron reduction is favoured over the further reduction to water. This is an indication that the adsorption of O_2 on the surface of our NOMCs is weaker compared to that on Pt, which is known to promote the dissociation of the O-O bond, thus leading to higher selectivity towards the complete reduction of oxygen to water [13].

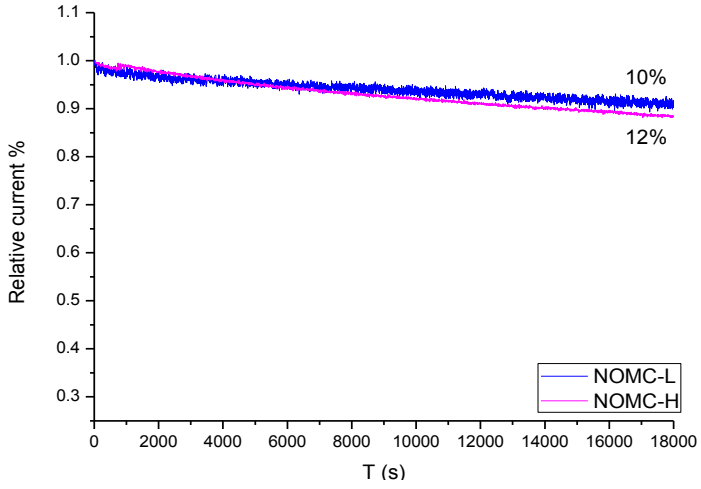

Figure 13. Relative current density vs. time (J-t) plot based on chronoamperometric measurements of NOMCs at -0.4 V vs. Ag/AgCl in O_2-saturated 0.1 M KOH at a rotation speed of 1600 rpm.

Finally, the stability of NOMC-L and NOMC-H was tested by chronoamperometric measurements at a constant potential of -0.4 V vs. Ag/AgCl for 5 h in a 0.1 M KOH solution saturated with O_2 at a rotation rate of 1600 rpm (Figure 13). Remarkably, the performance loss after 5 h was only 10% for NOMC-L and 12% for NOMC-H. This is the smallest degree of deactivation reported so far for NOMC electrocatalysts for the ORR, compared to the 15% decrease after 5 h observed with the optimum N-doped graphitic carbon material as electrocatalyst reported in the literature, and to the much more severe deactivation typically observed with standard Pt/C electrocatalysts [28, 50].

Conclusions

Metal-free N-doped ordered mesoporous carbon materials with high surface area and graphitic character were successfully prepared by means of a novel, two-step nanocasting method, and proved to be outstanding electrocatalysts for the oxygen reduction reaction. The NOMCs were synthesised with an accessible method using inexpensive N and C precursors (aniline and DHN), which is an important advantage towards the potential up-scaling of the fabrication of these materials. A careful control of the amounts of aniline and DHN and of the

synthesis conditions allowed preparing a material with a high N-content (up to 3.4 wt%) and a well-defined ordered mesoporous framework consisting of interconnected N-doped carbon rods with uniform size. The best NOMC electrocatalyst achieved a much superior kinetic current density in the ORR compared to previously reported N-doped carbon materials, and displayed high selectivity for a two-electron reduction process. This is highly promising for application in a fuel cell that could produce a useful chemical as H_2O_2 while cogenerating electricity. Importantly, a chronoamperometric test demonstrated that the optimum NOMC electrocatalyst also displays high long-term stability.

Acknowledgments

The authors acknowledge sponsoring from Flemish Agency for Innovation by Science and Technology (IWT) in the frame of an SBO project (OCPEC) and for a Ph.D. grant (ND), and the IAP-PAI research program. We thank Kitty Baert for helping with the XPS measurements, Prof. Jin Won Seo and the MTM department of the KU Leuven for their support in the TEM analyses and the Flemish Hercules Stichting for its support in HER/08/25, Prof. Christine Kirschhock and Dr. Eric Breynaert for the assistance in the SAXS analysis, Gina Vanbutsele and Dr. Lik Hong Wee for helping with the N_2-physisorption measurements. We thank Dr. Patrick Steegstra for useful discussion. Sara Bals acknowledges funding from the European Research Council under the 7th Framework Program (FP7), ERC Starting Grant No. 335078 COLOURATOMS.

References

[1] D. Geng, Y. Chen, Y. Chen, Y. Li, R. Li, X. Sun, S. Ye, S. Knights, High oxygen-reduction activity and durability of nitrogen-doped graphene, Energy Environ. Sci., 4 (2011) 760-764.

[2] X. Sheng, B. Wouters, T. Breugelmans, A. Hubin, F.J.I. Vankelecom, P.P. Pescarmona, Cu/Cu_xO and Pt nanoparticles supported on multi-walled carbon nanotubes as electrocatalysts for the reduction of nitrobenzene, Appl. Catal. B: Environ., 147 (2014) 330-339.

[3] W.C. Jones, H.J. Clark, Introduction to the preparation and properties of hydrogen peroxide, in: Applications of Hydrogen Peroxide and Derivatives, RSC, UK, 1999, pp. 1-36.

[4] I. Yamanaka, S. Tazawa, T. Murayama, T. Iwasaki, S. Takenaka, Catalytic synthesis of neutral hydrogen peroxide at a CoN_2C_x cathode of a polymer electrolyte membrane fuel cell (PEMFC), ChemSusChem, 3 (2010) 59-62.

[5] I. Yamanaka, T. Onizawa, S. Takenaka, K. Otsuka, Direct and continuous production of hydrogen peroxide with 93% selectivity using a fuel-cell system, Angew. Chem. Int. Ed., 42 (2003) 3653-3655.

[6] P. Landon, P.J. Collier, A.J. Papworth, C.J. Kiely, G.J. Hutchings, Direct formation of hydrogen peroxide from H_2/O_2 using a gold catalyst, Chem. Commun. , (2002) 2058-2059.

[7] S.J. Guo, S. Zhang, S.H. Sun, Tuning nanoparticle catalysis for the oxygen reduction reaction, Angew. Chem. Int. Ed., 52 (2013) 8526-8544.

[8] I. Yamanaka, S. Tazawa, T. Murayama, R. Ichihashi, N. Hanaizumi, Catalytic synthesis of neutral H_2O_2 solutions from O_2 and H_2 by a fuel cell reaction, ChemSusChem, 1 (2008) 988-992.

[9] T. Murayama, S. Tazawa, S. Takenaka, I. Yamanaka, Catalytic neutral hydrogen peroxide synthesis from O-2 and H-2 by PEMFC fuel, Catal. Today, 164 (2011) 163-168.

[10] H.A. Gasteiger, S.S. Kocha, B. Sompalli, F.T. Wagner, Activity benchmarks and requirements for Pt, Pt-alloy, and non-Pt oxygen reduction catalysts for PEMFCs, Appl. Catal. B: Environ., 56 (2005) 9-35.

[11] M. Schulze, N. Wagner, T. Kaz, K.A. Friedrich, Combined electrochemical and surface analysis investigation of degradation processes in polymer electrolyte membrane fuel cells, Electrochim. Acta 52 (2007) 2328-2336.

[12] E. Gülzow, M. Schulze, N. Wagner, T. Kaz, R. Reissner, G. Steinhilber, A. Schneider, Dry layer preparation and characterisation of polymer electrolyte fuel cell components, J. Power Sources, 86 (2000) 352-362.

[13] N. Daems, X. Sheng, I.F.J. Vankelecom, P.P. Pescarmona, Metal-free doped carbon materials as electrocatalysts for the oxygen reduction reaction J. Mater. Chem. A, 2 (2014) 4085-4110.

[14] G. Wu, K.L. More, C.M. Johnston, P. Zelenay, High-performance electrocatalysts for oxygen reduction derived from polyaniline, iron, and cobalt, Science, 332 (2011) 443-447.

[15] L. Wang, L. Zhang, J. Zhang, Optimizing catalyst loading in non-noble metal electrocatalyst layer to improve oxygen reduction reaction activity, Electrochem. Commun., 13 (2011) 447-449.

[16] T.-P. Fellinger, F. Hasché, P. Strasser, M. Antonietti, Mesoporous nitrogen-doped carbon for the electrocatalytic synthesis of hydrogen peroxide, J. Am. Chem. Soc., 134 (2012) 4072-4075.

[17] D.-W. Wang, D. Su, Heterogeneous nanocarbon materials for oxygen reduction reaction, Energy Environ. Sci., 7 (2014) 576–591.

[18] S. Mao, Z. Wen, T. Huang, Y. Hou, J. Chen, High-performance bi-functional electrocatalysts of 3D crumpled graphene–cobalt oxide nanohybrids for oxygen reduction and evolution reactions, Energy Environ. Sci., 7 (2014) 609-616.

[19] H. Wang, T. Maiyalagan, X. Wang, Review on recent progress in nitrogen-doped graphene: synthesis, characterization, and its potential applications, ACS Catal., 2 (2012) 781-794.

[20] N. Gokulakrishnan, N. Kania, B. Léger, C. Lancelot, D. Grosso, E. Monflier, A. Ponchel, An ordered hydrophobic P6mm mesoporous carbon with graphitic pore walls and its application in aqueous catalysis, Carbon, 49 (2011) 1290-1298.

[21] Y. Wang, F. Zhang, Y. Wang, J. Ren, C. Li, X. Liu, Y. Guo, Y. Guo, G. Lu, Synthesis of length controllable mesoporous SBA-15 rods, Mater. Chem. Phys, 115 (2009) 649-655.

[22] F. Rouquerol, J. Rouquerol, K. Sing, Chapter 6 - Assessment of Surface Area, in: F. Rouquerol, J. Rouquerol, K. Sing (Eds.) Adsorption by Powders and Porous Solids, Academic Press, London, 1999, pp. 165-189.

[23] C.F. Yu, S. Koh, J.E. Leisch, M.F. Toney, P. Strasser, Size and composition distribution dynamics of alloy nanoparticle electrocatalysts probed by anomalous small angle X-ray scattering (ASAXS), Faraday Discuss., 140 (2008) 283-296.

[24] J.J. Hernández, M.C. García-Gutiérrez, A. Nogales, D.R. Rueda, T.A. Ezquerra, Small-angle X-ray scattering of single-wall carbon nanotubes dispersed in molten poly(ethylene terephthalate), Compos. Sci. Technol., 66 (2006) 2629-2632.

[25] S. Lowell, E.J. Shields, Powder Surface Area and Porosity, 3rd ed., Chapman & Hall, New York, 1991.

[26] C. Carkeet, S.R. Dueker, J.R. Follett, T.E. Correa, A.J. Clifford, Carbon and nitrogen determinations using an isotope dilution ratio mass spectrometry approach, FASEB, 15 (2001) A260-A260.

[27] P. Gilbert, Iterative methods for the three-dimensional reconstruction of an object from projections, J. Theor. Biol., 36 (1972) 105-117.

[28] R. Liu, D. Wu, X. Feng, K. Müllen, Nitrogen-doped ordered mesoporous graphitic arrays with high electrocatalytic activity for oxygen reduction, Angew. Chem. Int. Ed., 49 (2010) 2565-2569.

[29] N. Liu, L. Yin, C. Wang, L. Zhang, N. Lun, D. Xiang, Y. Qi, R. Gao, Adjusting the texture and nitrogen content of ordered mesoporous nitrogen-doped carbon materials prepared using SBA-15 silica as a template, Carbon, 48 (2010) 3579-3591.

[30] Z.B. Lei, L.Z. An, L.Q. Dang, M.Y. Zhao, J.Y. Shi, S.Y. Bai, Y.D. Cao, Highly dispersed platinum supported on nitrogen-containing ordered mesoporous carbon for methanol electrochemical oxidation, Micropor. Mesopor. Mater., 119 (2009) 30-38.

[31] H. Nishihara, Y. Fukura, K. Inde, K. Tsuji, M. Takeuchi, T. Kyotani, Carbon-coated mesoporous silica with hydrophobicity and electrical conductivity, Carbon, 46 (2008) 48-53.

[32] W. Zou, X. Yuan, F. Zeng, X. Huang, S. Mo, D. Yuan, N-doped carbon nanowires synthesized from l-arginine for electrochemical application, Mater. Lett., 79 (2012) 195-198.

[33] H. Chang, S.H. Joo, C. Pak, Synthesis and characterization of mesoporous carbon for fuel cell applications J. Mater. Chem., 17 (2007) 3078-3088.

[34] C. Jin, G. Li, X. Wang, L. Zhao, Y. Wang, D. Sun, A Ti-containing molecular sieve assembled from titanosilicate precursors with long-chain alkylamines, Top. Catal., 49 (2008) 118-124.

[35] D.-H. Lin, Y.-X. Jiang, Y. Wang, S.-G. Sun, Silver nanoparticles confined in SBA-15 mesoporous silica and the application as a sensor for detecting hydrogen peroxide, J. Nanomater., (2008) 473791-473801.

[36] F. Rouquerol, J. Rouquerol, K. Sing, Chapter 7 - Assessment of Mesoporosity,, in: F. Rouquerol, J. Rouquerol, K. Sing (Eds.) Adsorption by Powders and Porous Solids, London, 1999, pp. 191-217.

[37] W. Schmidt, Calculation of XRD patterns of simulated FDU-15, CMK-5, and CMK-3 carbon structures, Micropor. Mesopor. Mater., 117 (2009) 372-379.

[38] K. Lund, N. Muroyama, O. Terasaki, Accidental extinction in powder XRD intensity of porous crystals: Mesoporous carbon crystal CMK-5 and layered zeolite-nanosheets, Micropor. Mesopor. Mater., 128 (2010) 71-77.

[39] Y.D. Xia, R. Mokaya, Generalized and facile synthesis approach to N-doped highly graphitic mesoporous carbon materials, Chem. Mater., 17 (2005) 1553-1560.

[40] I. Herrmann, U.I. Kramm, J. Radnik, S. Fiechter, P. Bogdanoff, Influence of sulfur on the pyrolysis of CoTMPP as electrocatalyst for the oxygen reduction reaction, J. Electrochem. Soc., 156 (2009) B1283-B1292.

[41] Y. Okamoto, First-principles molecular dynamics simulation of O_2 reduction on nitrogen-doped carbon, Appl. Surf. Sci., 256 (2009) 335-341.

[42] C. Zhang, R. Hao, H. Liao, Y. Hou, Synthesis of amino-functionalized graphene as metal-free catalyst and exploration of the roles of various nitrogen states in oxygen reduction reaction, Nano Energy, 2 (2013) 88-97.

[43] H. Kim, K. Lee, S.I. Woo, Y. Jung, On the mechanism of enhanced oxygen reduction reaction in nitrogen-doped graphene nanoribbons, Phys Chem Chem Phys., 13 (2011) 17505-17510.

[44] H. Liu, Y. Liu, D. Zhu, Chemical doping of graphene, J. Mater. Chem., 21 (2011) 3335-3345.

[45] Z. Luo, S. Lim, Z. Tian, J. Shang, L. Lai, B. MacDonald, C. Fu, Z. Shen, T. Yu, J. Lin, Pyridinic N doped graphene: synthesis, electronic structure, and electrocatalytic property, J. Mater. Chem., 21 (2011) 8038-8044.

[46] S. Tiva, H. Guangzhi, J. Xueen, W. Thomas, Formation of Active Sites for Oxygen Reduction Reactions by Transformation of Nitrogen Functionalities in Nitrogen-Doped Carbon Nanotubes, ACS Nano, 6 (2012) 8904-8912.

[47] J. Liang, Y. Jiao, M. Jaroniec, S. Qiao, Sulfur and nitrogen dual-doped mesoporous graphene electrocatalyst for oxygen reduction with synergistically enhanced performance, Angew. Chem. Int. Ed., 51 (2012) 11496-11500.

[48] Z.-H. Sheng, L. Shao, J.-J. Chen, W.-J. Bao, F.-B. Wang, X.-H. Xia, Catalyst-free synthesis of nitrogen-doped graphene via thermal annealing graphite oxide with melamine and its excellent electrocatalysis, ACS Nano, 5 (2011) 4350-4358.

[49] M.N. Zhang, Y.M. Yan, K.P. Gong, L.Q. Mao, Z.X. Guo, Y. Chen, Electrostatic layer-by-layer assembled carbon nanotube multilayer film and its electrocatalytic activity for O_2 reduction, Langmuir, 20 (2004) 8781-8785.

[50] P. Zhang, F. Sun, Z. Xiang, Z. Shen, J. Yunb, D. Cao, ZIF-derived in situ nitrogen-doped porous carbons as efficient metal-free electrocatalysts for oxygen reduction reaction, Energy Environ. Sci., 7 (2014) 442-450.

[51] X.Q. Wang, J.S. Lee, Q. Zhu, J. Liu, Y. Wang, S. Dai, Ammonia-treated ordered mesoporous carbons as catalytic materials for oxygen reduction reaction, Chem. Mater., 22 (2010) 2178-2180.

[52] Y. Zhang, K. Fugane, T. Mori, L. Niu, J. Ye, Wet chemical synthesis of nitrogen-doped graphene towards oxygen reduction electrocatalysts without high-temperateure pyrolysis, J. Mater. Chem. , 22 (2012) 6575-6580.

[53] Q. Li, R. Cao, J. Cho, G. Wu, Nanocarbon Electrocatalysts for Oxygen Reduction in Alkaline Media for Advanced Energy Conversion and Storage, Adv. Energy Mater. , 4 (2014) 1301415 (1-19).